Cytometry
PART A
Journal of the International Society for Advancement of Cytometry

Statistical Analysis of Molecule Colocalization in Bioimaging

Thibault Lagache,[1]* Nathalie Sauvonnet,[2] Lydia Danglot,[3] Jean-Christophe Olivo-Marin[1]*

[1]Cell Biology and Infection Department, BioImage Analysis Unit, Institut Pasteur, 75724 Paris Cedex 15, France

[2]Cell Biology and Infection Department, Molecular Microbial Pathogenesis Unit, Institut Pasteur, 75724 Paris Cedex 15, France

[3]Membrane trafic in Heath and Disease Unit - Inserm 950. Institut Jacques Monod - CNRS UMR7592, Université Paris Diderot, 75205 Paris Cedex 13, France

Received 15 July 2014; Revised 19 December 2014; Accepted 28 December 2014

Grant sponsor: Agence Nationale de la Recherche (ANR-10-INBS-04-06 France-BioImaging and ANR-10-LABX-62-IBEID; Grant sponsor: Bourse Roux and PTR 387 from Institut Pasteur; Grant sponsor: Institut pour la Recherche sur la Moelle et l'Encéphale

*Correspondence to: Thibault Lagache, BioImage Analysis Unit, Cell Biology and Infection Department, Institut Pasteur, 75724 Paris Cedex 15, France. E-mail: thibault.lagache@pasteur.fr (or) Jean-Christophe Olivo-Marin, BioImage Analysis Unit, Cell Biology and Infection Department, Institut Pasteur, 75724 Paris Cedex 15, France.
E-mail: jcolivo@pasteur.fr

Published online 00 Month 2015 in Wiley Online Library (wileyonlinelibrary.com)

DOI: 10.1002/cyto.a.22629

Abstract

The quantitative analysis of molecule interactions in bioimaging is key for understanding the molecular orchestration of cellular processes and is generally achieved through the study of the spatial colocalization between the different populations of molecules. Colocalization methods are traditionally divided into pixel-based methods that measure global correlation coefficients from the overlap between pixel intensities in different color channels, and object-based methods that first segment molecule spots and then analyze their spatial distributions with second-order statistics. Here, we present a review of such colocalization methods and give a quantitative comparison of their relative merits in different types of biological applications and contexts. We show on synthetic and biological images that object-based methods are more robust statistically than pixel-based methods, and allow moreover to quantify accurately the number of colocalized molecules. © 2015 International Society for Advancement of Cytometry

Key terms

spatial statistics; colocalization; quantitative measurements; light microscopy; endocytosis

Quantitative measurement of molecules interactions in cellular biology is a key step toward the understanding of molecular processes orchestration, such as endocytosis (1), and their hijacking by bacteria (2) and viruses (3). In fluorescence microscopy, the measurement of molecule interactions can be monitored through several techniques, like Förster resonance energy transfer (FRET) (4) or Fluorescence Cross-Correlation Spectroscopy (FCCS) (5). However, FRET cannot be used when interacting molecules are too large, when they are part of a macromolecular complex (indirect interaction), or when molecules only colocalize spatially in cellular microdomains such as membrane domains or intracellular organelles (endosomes, . . .; see Fig. 1). In addition, FCCS cannot be applied when one of the molecules is docked or immobilized. Last but not least, these methods are difficult to use for the analysis of the interaction between more than two different molecule populations (6) and cannot benefit from multispectral color imaging of multiple chromophores attached to different molecules (7). For all these reasons, the analysis of molecule interactions is performed generally through the quantification of their spatial colocalization in the microscope's field of view (FOV; (8)).

Classical colocalization methods are based on the analysis of the pixel-wise correlation between the signals emitted in two or more color channels corresponding to the fluorescence wavelength of the labels (see Fig. 2). These pixel-based methods have given rise to a large number of different correlation coefficients (8), the mostly used being Pearson's and Manders' coefficients (8–10). More recently, object-based methods, which segment the individual molecules (objects), before analyzing their spatial distribution, have been introduced (11–16; see Fig. 2). In the latter case, different statistics are used for spatial analysis. Most used statistics are second-order statistics and are based on distances between neighbor points. In the first part of this

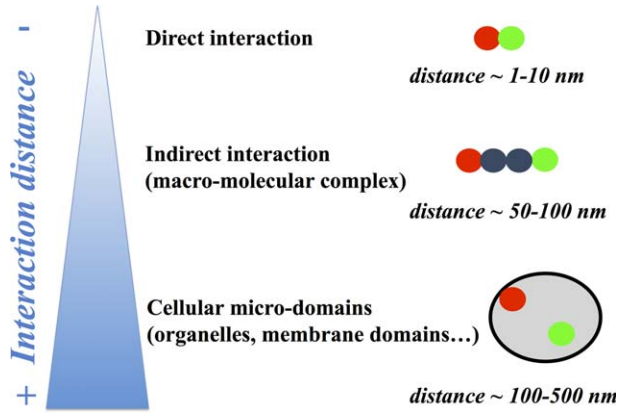

Figure 1. Different molecule interactions. Molecule (green and red dots) can interact directly at small distance ~1−10 nm, but their size or their indirect interaction in large molecular complexes (blue dots) lead to much larger interaction distances ~10−100 nm. Colocalization analysis can also be used to assess mutual presence of molecules in membrane microdomains or intracellular organelles. The resulting interaction distance can then reach the organelle size ~500 nm. [Color figure can be viewed in the online issue, which is available at wileyonlinelibrary.com.]

review, we will present in detail the different pixel- and object-based methods that have been developed over the years. For each of these methods, we will discuss whether they are able to handle the two following important technical issues:

1. Statistical Robustness: Is the Observed Colocalization Significant? Even for a random molecule spatial distribution, spatial colocalization can occur by chance. These fortuitous colocalization events increase with molecule density in the microscope FOV, and it is therefore important to test statistically whether the measured colocalization is statistically relevant. We highlight that the null hypothesis of molecule" non-colocalization" is not easy to define. Thus, in practice, the null hypothesis of molecule random distribution is mainly used, even if this condition is stronger than just" non-colocalization". Indeed, molecules can be independently distributed without being randomly distributed.
2. Quantification Accuracy: Can the Percentage of Colocalized Molecules and Their Distances be Inferred from the Colocalization Method? The number of colocalized molecules gives important information about the interaction strength and stoichiometry, and the colocalization distance reveals the nature of the interaction [direct, indirect, closeby in the same organelle (see Fig. 1)]. However, as we will see hereafter, the quantitative interpretation of the correlation coefficients and spatial statistics is rarely straightforward, meaning that additional analysis is required to extract quantitative information such as the number of colocalized molecules, or their distance.

Following the detailed and critical presentation of mostly used pixel-based and object-based methods, we will compare the different methods on synthetic and biological images. For this, we will first analyze how the main pixel-based and object-based methods perform on synthetic images with different level of noise and (known) percentage of colocalization. Then, we will use the different methods to measure the colocalization at the cell membrane between two cargos that enter

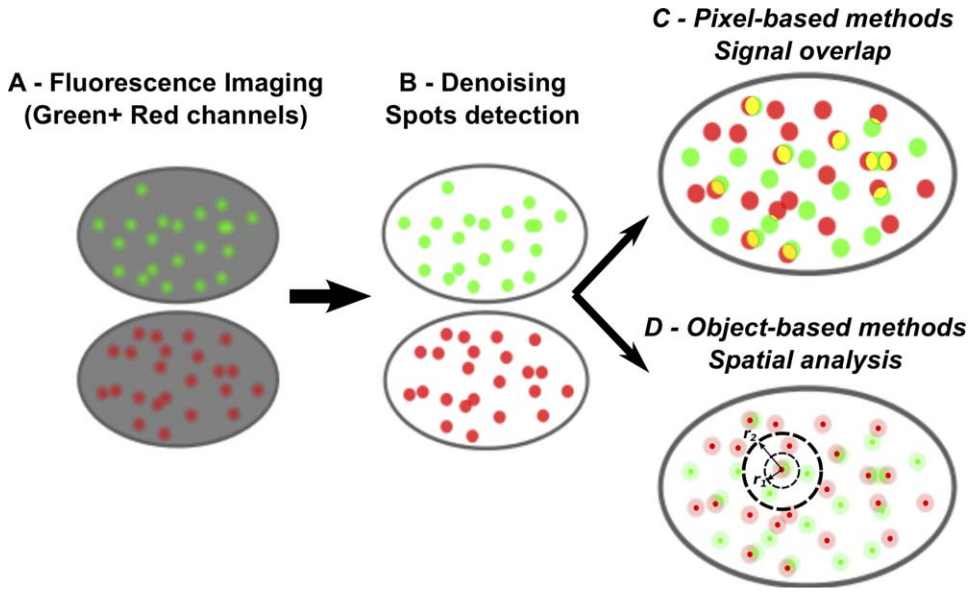

Figure 2. Principles of colocalization analysis in fluorescence microscopy. **A**: Molecules are visualized in a dual-channel fluorescence image. **B**: Images are de-noised and fluorescent spots corresponding to molecule signal are extracted automatically with wavelet detection method (22). **C**: In pixel-based methods, molecule colocalization is analyzed by measuring the overlap between de-noised signal with correlation coefficients, such as the Pearson (10) and Manders (9) coefficients. **D**: In object-based methods, molecule spots are first segmented and represented as points through the coordinates of their center of mass in the FOV. Then, second-order statistics such as distance to nearest neighbor (42), or Ripley's K function (43) are used to analyze point spatial distributions. [Color figure can be viewed in the online issue, which is available at wileyonlinelibrary.com.]

the cell through endocytosis, the transferrin (Tf) and interleukin-2 receptor (IL-2R), with intracellular molecules that are implicated in different endocytic pathways.

Materials and Methods

Experimental Protocol, TIRF Microscopy

Hep2β cells expressing IL-2R (17) were grown in DMEM containing 10% FCS and 1 mg/mL of geneticin (Gibco). We used clathrin-light chain (CLC) and caveolin 1 all tagged to GFP (18,19) to transfect them into Hep2β cells (19). To image the two cargos, 1 $\times$ 105 Hep2β cells transfected with either CLC-GFP or Cav1-GFP and plated on MatTek plates, were incubated 2 min with either Tf-Cy3 or anti-IL-2Rβ-Cy3 in a TIRF medium (25 mM Hepes, 135 mM NaCl, 5 mM KCl, 1.8 mM CaCl2, 0.4 mM MgCl2, 4.5 g/L glucose, pH 7.4, and 0.5% BSA) at 37°C, washed and fixed (19). Experiments were performed using a TIRF microscope (IX81F-3, Olympus) equipped with a 100x NA 1.45 Plan Apo TIRFM Objective (Olympus) and fully controlled by CellM (Olympus). Two solid-state laser lines (488 and 561 nm; Olympus) were coupled to a TIRF condenser through two optical fibers. The two color channels were simultaneously acquired through a Dual View beam splitter (Optical Insights), to separate the two emission signals to two sides of the camera, using a 565 nm dichroic mirror and 525/50 and 605/55 nm emission filters. Images were collected using an IxonEM+ Camera (DU885, Andor).

Synthetic Image Generation and Image Analysis

We used a Mixed Poisson-Gaussian model to generate synthetic fluorescent images (see chapter 1 of Ref. 20). In this model, the intensity $I[x, y]$ at pixel location $[x, y]$ is equal to $I[x, y] = \text{gain} * U[x, y] + N(x, y)$ where U is a random Poisson variable and N an additive white Gaussian noise with mean 0 and standard deviation equal to 3. The mean $\lambda[x, y]$ of the Poisson variable U varies spatially: $\lambda[x, y] = P[x, y] + B$, $P[x, y]$ being the sum of the intensity of the particles generated in $[x, y]$ and $B = 10$ a constant background value. gain $= 1$ is the gain of the acquisition system. Finally, we assumed an additive model for the intensity of the particles: $P[x, y] = \sum_{i=1}^{N} P_i[x, y]$, where $P_i[x, y]$ is the signal originating from the ith particle in pixel $[x, y]$. When a particle is significantly smaller than the resolution of the microscope, its intensity profile P_i is well represented by the Gaussian point spread function (PSF) of the microscope (21) with a specific amplitude A_i: $P_i[x, y] = A_i e^{-\frac{(x-x_i^0)^2+(y-y_i^0)^2}{2\sigma_{xy}^2}}$ where $[x_i^0, y_i^0]$ is the coordinate of the ith particle and σ_{xy} the standard deviation of the 2D Gaussian profile of the PSF. We sampled uniformly A_i between 20 and 25 for each particle $1 \leq i \leq N$.

In synthetic and biological images, we used a wavelet-based detection method (22), implemented in the plugin Spot detector in the Icy platform (23) (http://icy.bioimageanalysis.org) to extract molecule signals that are statistically brighter than background. Molecule position $[x, y]$ was then inferred from centroids of detected spots.

Pixel-Based Methods

Principle

The first quantitative methods were introduced in the 90's and were pixel-based (9,24–26). They are based on the computation of correlation coefficients between pixel intensities in the different channels. In most studies, a preliminary de-noising of the image is performed to remove noise from the correlation analysis (see Fig. 2). Denoising can be based on hard thresholding the image, keeping pixels with intensity above given threshold, or it can use more elaborated techniques such as wavelet thresholding (22). Hereafter, we present the principal correlation coefficients that are used in pixel-based methods.

The first correlation coefficient to be used was the Pearson coefficient R (24–26). Denoting I_1^i and I_2^i the intensities of pixel $1 \leq i \leq n$ in microscope channels 1 and 2, the mathematical expression of the Pearson coefficient is $R = \frac{\overline{I_1 I_2} - \overline{I_1}\,\overline{I_2}}{\sigma(I_1)\sigma(I_2)}$, where the bar stands for the mean, and $\sigma(I_j)$, $j = 1, 2$, is the standard deviation of pixel intensities in each channel. Conceptually, Pearson's coefficient measures the part of the measured variations in one channel that can be explained by variations in the other channel, and it ranges between -1 and 1. The extreme values -1 and 1 indicate respectively perfect anti-correlation and correlation, whereas $R = 0$ means that channels are not correlated. The Pearson coefficient determines actually signal correlation, not colocalization. Thus, the quantitative interpretation of intermediate values of the Pearson's coefficient is not easy. To tackle this issue, van Steensel et al. proposed (24) to compare the coefficient with the values that are obtained after a shift of δx pixels of the first channel. Then, if the maximum value of R is obtained with no shift $\delta x = 0$, it means that that channels correlate, whereas if R does not change with δx, or is minimal at $\delta x = 0$, it indicates that channels do not correlate, or are segregated.

The other correlation coefficients to be highly used are Mander's coefficients (9) that measure the amount of channel 1 (M_1 coefficient) and channel 2 (M_2 coefficient) signal that colocalize with other channel: $M_1 = \frac{\sum_{i=1}^{n} I_{1,\text{coloc}}^i}{\sum_{i=1}^{n} I_1^i}$ and $M_2 = \frac{\sum_{i=1}^{n} I_{2,\text{coloc}}^i}{\sum_{i=1}^{n} I_2^i}$, where $\sum_{i=1}^{n} I_{j,\text{coloc}}^i$, for $j = 1, 2$, is the total intensity of channel j pixels I_j^i that colocalize with bright, denoised pixels of the other channel. Quantitative interpretation of Mander's coefficients is much more straight forward than Pearson coefficient. Indeed, $M_j = x\%$ means that $x\%$ of channel j signal colocalize with signal in the other channel. In addition, Mander's coefficient allow to analyze channels separately.

Statistical Robustness

Partial colocalization between fluorescent spots can happen even for randomly distributed molecules, and consequently, it is important to test statistically the significance of computed correlation coefficients. For this, the first step is to define the null hypothesis of the colocalization test, which is in most studies, the random distribution of pixels in each image channel (10,25,27). Then, the second step of the statistical analysis is the determination of the level of significance of the computed correlation coefficient. A simple method is

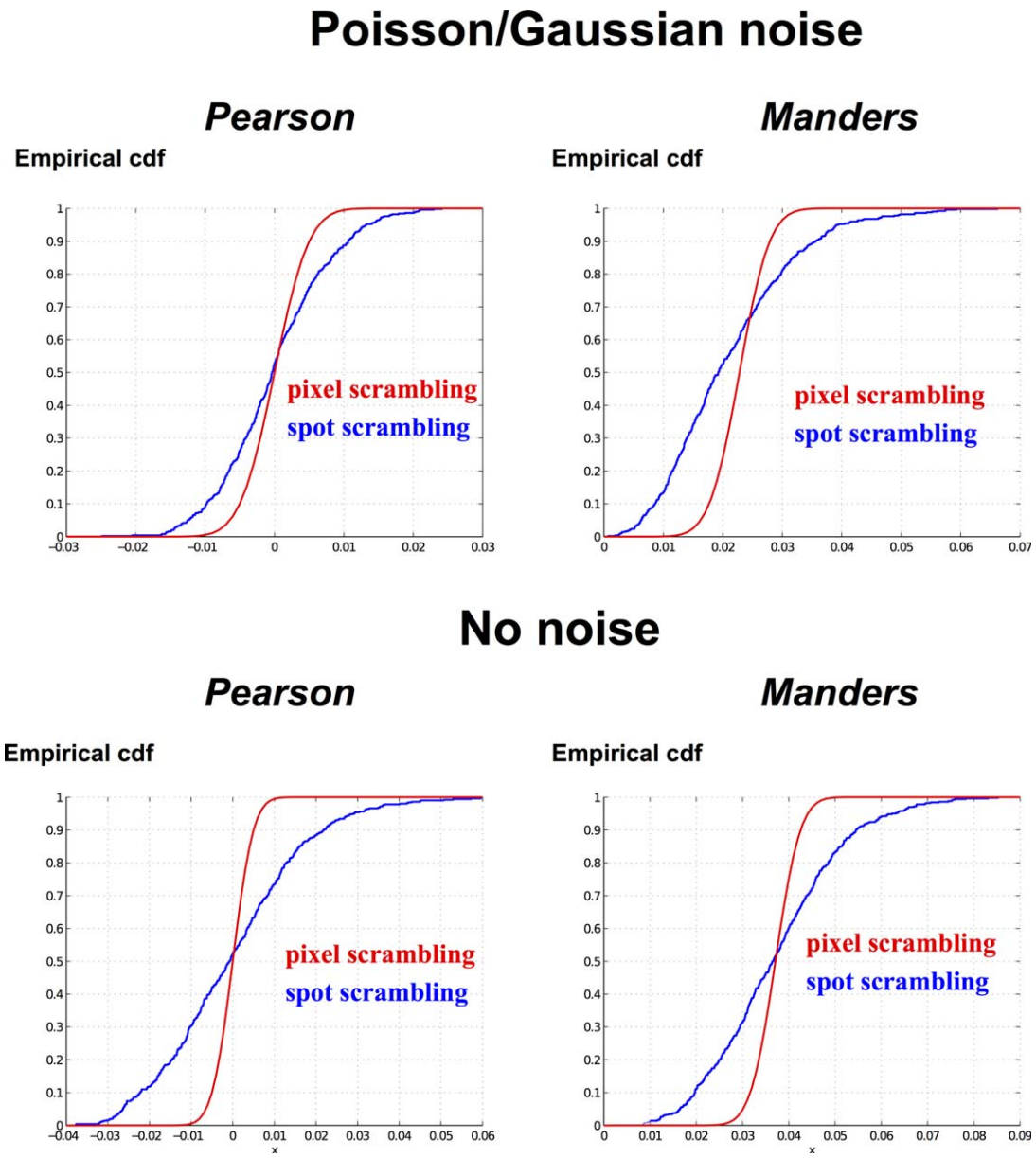

Figure 3. Empirical cumulative density function (CDF) of Pearson and Manders correlation coefficients. Dual-color synthetic images containing $n_1 = n_2 = 100$ spots are generated with a Poisson-Gaussian model (see Material and Methods). For the computation of Manders coefficients, fluorescent spots are first automatically segmented with a wavelet-based algorithm (22). Empirical CDF of Pearson and Manders correlation coefficients are then obtained with either pixel or spot randomization ($N = 500$ Monte-Carlo simulations). [Color figure can be viewed in the online issue, which is available at wileyonlinelibrary.com.]

based on multiple ($M >> 1$) pixel randomizations in the FOV for each channel. Indeed, by computing the correlation coefficient at each randomization ($X(i),\ 1 \leq i \leq M, X = R, M_1, M_2 \ldots$) and by sorting the different computed values ($X(1) \leq \ldots \leq X(M)$), one can then approximate the quantile $q_{1-\alpha}$ at level $1-\alpha$ of the correlation coefficient under the null hypothesis with $X(\lfloor (1-\alpha)M \rfloor)$, where $\lfloor . \rfloor$ is the floor function. We highlight that pixel random distribution does not correspond to molecule random distribution. Indeed, even for randomly distributed molecules, pixels are not statistically independent data points. Instead, they are autocorrelated (each pixel is likely to have similar values to its neighboring pixels), and the primary source of autocorrelation is the point- spread function of the imaging system, which spreads the signal of point sources to round shape pixel aggregates (spots; 28). This technical issue is discussed in (10), where Costes et al. propose to randomize pixels block, block size being approximately equal to molecule spot size, to simulate molecule randomization. However, block scrambling nevertheless reduces pixel autocorrelation compared to natural images, leading to false colocalization detection in random data (29). Using synthetic fluorescence images with randomly

distributed spots instead of pixel scrambling, Ramirez et al. demonstrated that the probability density functions (PDFs) for Manders and Pearson correlation coefficients were significantly different (Fig. 4 in Ref. 30). In particular, the variance of the PDF obtained with spot scrambling increased with spot randomization instead of pixel scrambling, leading to the conclusion that false positives were observed with pixel scrambling. We confirmed here these results by generating synthetic images with $n_1 = n_2 = 100$ spots randomly distributed in a 256×256 pixels FOV (see Material and Methods), and comparing the cumulative density functions (CDFs) of Pearson and Manders coefficients computed empirically with either pixel or spot randomization (Fig. 3). We observed that CDFs were significantly sharper with pixel randomization, and reached significantly high values (>0.95) at points where CDFs obtained with spot randomization are around 0.80 (with Poisson/Gaussian noise) or 0.65 (no noise) only. Thus, we confirmed that pixel randomization leads to false positive colocalization compared to spot randomization (29). Finally, we underline that spot randomization is based on synthetic images, and requires to define and estimate image model parameters (noise, intensity, number of spots; (6,30,31)).

The major drawback of spot randomization methods is the robust estimation of synthetic image parameters (number and shape of spots, noise ...). In addition, the computational load of pixel and spot randomization can hinder its use on large images and time-lapse imaging. Li et al. tackled partially this latter issue by proposing a statistical test that does not need pixel randomization (27). For this, they first introduced the Pearson-derived, intensity-correlation coefficient $\tilde{R} = \sigma(I_1)\sigma(I_2)R = \overline{I_1 I_2} - \overline{I_1}\,\overline{I_2}$, and proposed to use the intensity correlation quotient (ICQ) $\mathrm{ICQ} = \frac{1}{n}\sum_{i=1}^{n} \mathbf{1}(\tilde{R}^i > 0) - 0.5$ as a test statistics of pixel random distribution. Indeed, they claim that ICQ is centered around 0 when pixels are randomly distributed, whereas signal colocalization shifts the ICQ to positive values ($0 < \mathrm{ICQ} < 0.5$). Thus, using the fact that the probability $\Pr\{\mathrm{ICQ} > 0\} = 0.5$ under the null hypothesis of pixel random distribution, they measure the significance of the empirical ICQ by using a nonparametric sign test. We highlight that the hypothesis that $\Pr\{\mathrm{ICQ} > 0\} = 0.5$ when pixels are randomly distributed holds when the pixel intensity distribution is symmetric (skewness = 0), which is not the case, for example, when signal intensity is low.

Finally, when m multiple images are acquired in same experimental conditions, McDonald and Dunn proposed to use a one sample Student's t test ($m-2$ degrees of freedom) of whether the mean Pearson coefficient $\bar{R} = \frac{1}{m}\sum_{p=1}^{p=m} R_p$ is statistically > 0 (28). This solves the technical issue of pixel autocorrelation as whole images are used for the test. In addition, McDonald and Dunn confirmed the statistical power of the t test on synthetic data (28).

Quantitative Interpretation

The quantitative interpretation of pixel correlation coefficients is very difficult, representing the major drawback of pixel-based methods. Indeed, partial overlap of molecule spot can appear by chance, particularly when spots are large and the density of molecules in the FOV is high. Conversely, it is rare that spots of colocalized molecules overlap perfectly (see Fig. 2), due to the variability of spot shapes and the nonzero distance between colocalized molecules, which results from the sum of the physical interaction distance (see Fig. 1), the molecule localization error (32) and potential mis-alignment of microscope channels. In addition, the physical distance between colocalized molecules is rarely zero and the overlap of their spots is drastically decreased when the spot size is reduced with super-resolution techniques such as structured illumination (33) or STED microscopy (34). For all these reasons, overlap percentage obtained with Manders correlation coefficients (9) is hardly convertible into molecule colocalization. Intensity cross-correlation spectroscopy (ICCS) tackled partially this issue by estimating the percentage p_k of molecules k that colocalize with other molecules ($k = 1, 2$) from of Pearson-based ratio $p_k \approx \frac{r}{r_k}$, with $r = \frac{\sigma(I_1)\sigma(I_2)}{\overline{I_1}\,\overline{I_2}} R$ and $r_k = \frac{\sigma^2(I_k)}{\overline{I_k}^2} R$ (35,36). When comparing colocalization methods with synthetic images, we used the previous formula for p_k, but we highlight that p_k computation accuracy can be improved by fitting the spatial variations (u, v) of the ratio $\frac{r}{r_k}(u, v)$ with a Gaussian distribution: $\frac{r}{r_k}(u, v) = \frac{r}{r_k}(0, 0) e^{-\frac{u^2+v^2}{2\sigma^2}} + a_\infty$, where a_∞ is a constant, and by setting $p_k \approx \frac{r}{r_k}(0, 0)$ (35,36).

Finally, the mean distance between colocalized spots is hardly accessible from pixel correlation coefficients. In addition, Pixel-based methods are not compatible with super-resolution localization microscopy [PALM (37) or STORM (38)], which infer directly the molecule position from sequential activation of multiple photo-switchable fluorophores attached to molecules. These super-resolution advances explain partially the recent development of object-based methods, which are based on the spatial analysis of molecule localizations.

Object-Based Methods

Principle

In object-based methods, the molecules (objects) are first segmented and are then represented as points through coordinates of their mass center in the delimited FOV (see Fig. 4A). These methods do not depend on spot size and are particularly well-suited for super-resolution localization microscopy that infer directly molecule positions from multiple photoactivable fluorophores (37,38). However, in all microscopes, these methods rise a first technical issue, which consists in detecting and segmenting molecule spots. This can be achieved with wavelet based methods (22) and point-spread function fitting (39), which have demonstrated their robustness even in very noisy images (40). Then, the mathematical framework of Marked Point Process (41), where the mark is the type (color) of point (molecule), is particularly adapted to analyze the relations between the spatial distributions of the two populations (see Fig. 4B). Indeed, the first statistical question that arises is whether points are randomly distributed (42,43), or equivalently, if the observed point distributions can be modeled by a uniform Poisson point process. As a matter of fact, a randomly

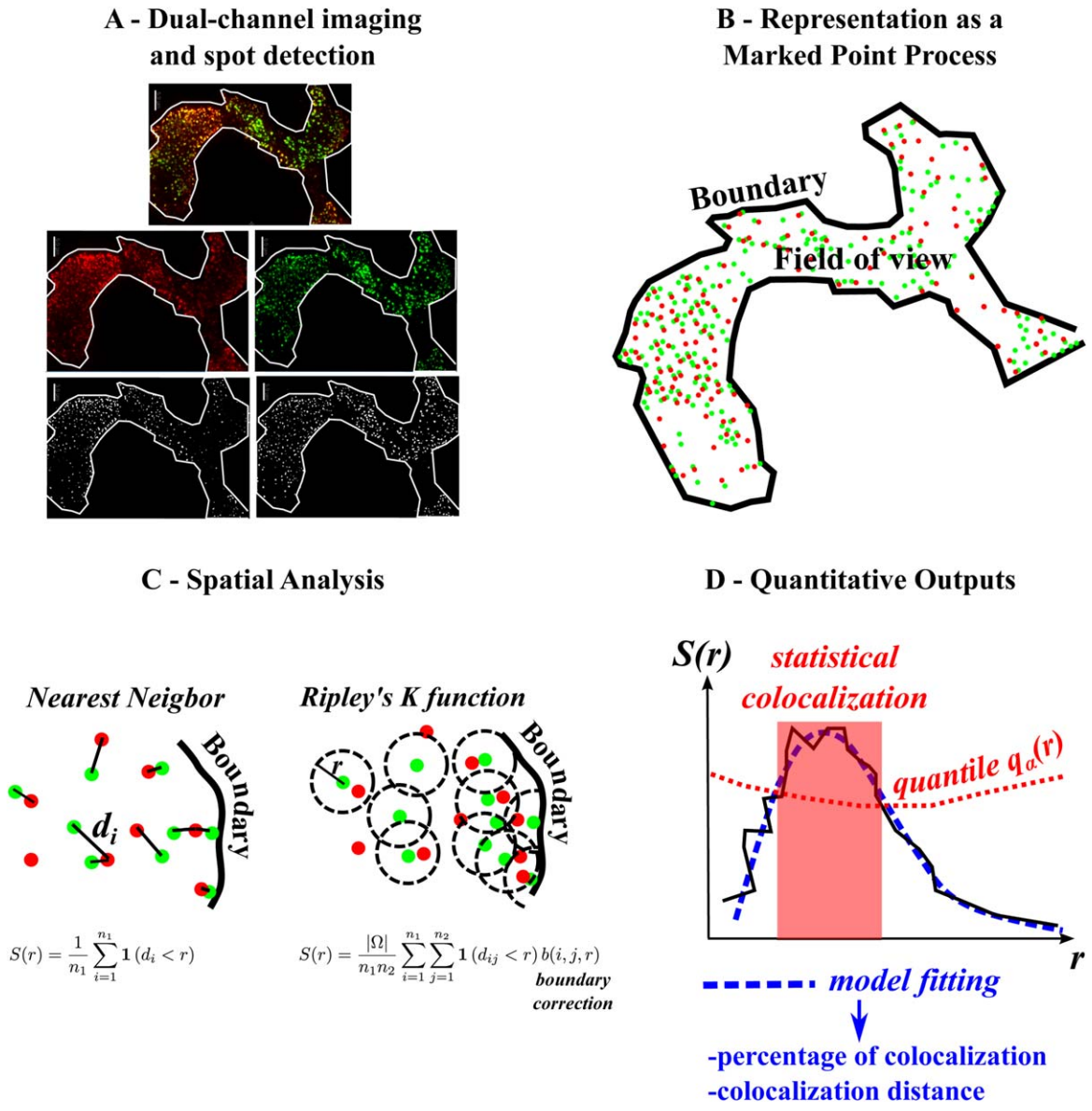

Figure 4. Object-based statistical analysis. **A**: Punctuated fluorescent molecules are segmented automatically in the different color channels, and are represented as points through the coordinates of their center of mass in the FOV. **B**: Mathematical formalism of Marked-Point-Processes (41) is used to represent the molecule positions in the delimited FOV, the mark being the color of the molecule. **C**: Second-order statistics $S(r)$ such as the the distance to nearest-neighbor (42) and the Ripley's K function (43) allow to analyze the spatial distribution of marked points. In Ripley-based analysis, a boundary correction $b(i,j,r)$ prevents bias in $S(r)$ due to neighbor underestimation at larger values of r. **D**: Colocalization is statistically assessed through the comparison of the computed second-order statistics $S(r)$ (black solid line) with its critical quantiles $q_{1-\alpha}(r)$ at level $1-\alpha$ under the null hypothesis of point random distribution (red dashed line). The percentage of colocalization, and the distance between colocalized points is inferred from parametrical fitting of $S(r)$ (blue dashed line). [Color figure can be viewed in the online issue, which is available at wileyonlinelibrary.com.]

distributed point process can fall in the neighborhood of another point process, leading to fortuitous colocalization events. It is therefore important to measure the statistical relevance of the colocalization occurrence. The second major issue when analyzing Marked Point Processes is the robust quantification of the percentage and the distance of point colocalization from their spatial distribution.

Analysis of Marked Point Processes is mostly based on second-order, descriptive statistics which try to capture information about the distance between points and their neighbors. In that context, the tools of reference are the distance to nearest-neighbor (42), and Ripley's K function (43) and its derivative, the pair correlation function (44,45; see Fig. 4C). In nearest-neighbor based method, the test statistic S is based on distance d_i of each point of the first population A_1 (n_1 points) to nearest-neighbor in the second A_2 population (n_2 points) (see Fig. 4C). In its simplest form, test statistic S is the mean distance to nearest neighbors $S = \frac{1}{n_1}\sum_{i=1}^{n_1} d_i$ (42),

but more complex statistics, that enable multidistance analysis, have been introduced over years. In particular, the nearest-neighbor function $S(r) = \frac{1}{n_1}\sum_{i=1}^{n_1} \mathbf{1}(d_i < r)$ allows to test whether points colocalize at distances below the parameter r (14,46). In Ripley-based analysis, the test statistic is the Ripley's K function, or its derivative the pair correlation function. For a distance parameter r and delimited FOV Ω, the standard expression of the Ripley's K function is $S(r) = \frac{|\Omega|}{n_1 n_2} \sum_{i=1}^{n_1}\sum_{j=1}^{n_2} \mathbf{1}(d_{ij} < r) b(i,j,r)$ where $|\Omega|$ is the area or the volume of Ω, d_{ij} the euclidian distance between point i of first population A_1 and point j of second population A_2, and $b(i, j, r)$ is a boundary correction term that prevents a bias in $S(r)$ due to neighbor underestimation at larger values of r (see Fig. 4C). Indeed, under the assumption of A_2 random distribution, points in A_1 that are close to the FOV boundary will have less neighbors than the others (typically, a point located on, or very close to, the boundary will have, on average, half of the neighbors than a point located far from the boundary). Surprisingly, boundary correction is not used in nearest-neighbor approach, while many different forms of corrections have been proposed for Ripley-based statistics. In particular, the Ripley's correction is one of the most standard corrections in spatial analysis and is given by $b(i,j,r) = |c(i,d_{ij})|/|c(i,d_{ij}) \cap \Omega|$, where $c(i,d_{ij})$ is the circle (sphere) centered at i with radius d_{ij}. We highlight that for a point i located at the boundary, $b(i,j,r) \approx 2$.

Statistical Robustness

Statistical test of molecule (point) colocalization is mostly achieved through the comparison of the second-order statistics $S(r)$ with the critical quantiles $q_{1-\alpha}(r)$ at level $1-\alpha$ under the null hypothesis of molecule random distribution in the FOV (see Fig. 4D). We note that comparison between $S(r)$ and $q_{1-\alpha}(r)$ at several distances r allows to determine the distances where the Ripley- or Nearest-Neighbor-based statistics $S(r)$ exit the critical envelope $q_{1-\alpha}(r)$, indicating at which distances points co-localize statistically (see Fig. 4D).

In the theoretical case when the FOV is not limited, the probability density function of most second-order statistics has been characterized under the null hypothesis of A_2 molecule random distribution. For example, the null distribution of the nearest neighbor function $S(r) = \frac{1}{n_1}\sum_{i=1}^{n_1} \mathbf{1}(d_i < r)$ is equal to $1-e^{-\frac{n_2}{|\Omega|}B(r)}$, where $B(r)$ is the area of the ball with radius r, that is $B(r) = \pi r^2$ in two dimensions and $B(r) = \frac{4}{3}\pi r^3$ in three dimensions. Conversely, in delimited FOVs, there are very few statistical results as it is difficult to account for the contour geometry. Indeed, the underestimation of neighbors for points close to the FOV boundary, even with corrections, modifies the probabilistic distribution of Ripley-based or nearest-neigbors statistics, and no, or only few analytical characterization of these geometry-constrained laws have been proposed (47–49). Consequently, the quantiles of descriptive statistics under the null hypothesis of point random distribution, that are needed to assess statistically whether point colocalize or not, are computed with Monte-Carlo simulations in each FOV (11–14). Even if it answers the need for statistical robustness of the method, it induces a high computational load, and requires calibration. Recently, we tackled partially this issue in (15) by characterizing the probability distribution of the Ripley's K function under the null hypothesis, and as a function of the geometry of the FOV. We demonstrated that the K function is asymptotically normal $S(r) \sim \mathcal{N}(\mu(r), \sigma(r))$ for $n_1 n_2 >> 1$, and we computed that, using the Ripley's boundary correction, $\mu(r) = B(r)$, and that $\sigma^2(r) = \frac{|\Omega|}{n_1^2 n_2}(\sum_{i=1}^{n_1}\beta_i + \sum_{k\neq i} A_{ik}) - \frac{B(r)^2}{n_2}$, where β_i is function of the distance $|i-\partial\Omega|$ of each point i to the boundary $\partial\Omega$, and A_{ik} is the area of the intersection of balls centered at $i \neq k$. Critical quantiles $q_{1-\alpha}(r)$ of $S(r)$ are then given by $q_{1-\alpha}(r) = \mu(r) + \sigma(r) z_{1-\alpha}$, where $z_{1-\alpha}$ is the quantile of the standard normal law $\mathcal{N}(0,1)$.

Finally, we note that testing separately $S(r)$ against $q_{1-\alpha}(r)$ for different r does not provide the exact probability that the observed points interact or equivalently, that they are not the realizations of random Poisson processes. Indeed, second-order statistics (Nearest-Neighbor or Ripley's K functions) $S(r_i)$ and $S(r_j)$, for $1 \leq i \neq j \leq N$, are correlated random variables, and a statistical test that accounts globally for the multidistance information $S(r_i)$, for $r_1 < \ldots < r_i < \ldots < r_N$ is required. To elaborate such a statistical test, an essential prerequisite is to construct a summary statistics that accounts for the correlations at different distances and recapitulates the multidistance information in a single statistics. In the context of nearest-neighbor methods, Sbalzarini and coworkers introduced the distance counts $\mathbf{T} = (T_1, \ldots, T_L)^t$, where $T_j = \sum_{i=1}^{n_1} \mathbf{1}(r_j \leq d_i < r_{j+1})$. Then, they proposed the summary test statistic $U = (\mathbf{E}_0(\mathbf{T}) - \mathbf{T})^t \mathbf{Cov}_0(\mathbf{T})^{-1} (\mathbf{E}_0(\mathbf{T}) - \mathbf{T})$, where $\mathbf{E}_0(\mathbf{T})$ and $\mathbf{Cov}_0$ are the empirical mean and variance of $\mathbf{T}$ obtained with simulations. We were not able to exhibit similar summary statistics for Ripley-based statistics. However, for a single population of molecules, we highlight that Lang and Marcon computed analytically the covariance of Ripley's K function at different distances in the unit square, and using the normal convergence of the K function, they proposed to use a χ^2 global test of molecule positions randomness (47). The computation of the K function covariance for two populations of points and any FOV, which can be achieved with simulations in a first step, would allow to extend χ^2 tests to colocalization analysis.

Quantitative Interpretation

A second important issue when analyzing second-order statistics is the quantification of detected spatial colocalization. In the field of bioimaging, among the relatively few methods that have been proposed an important contribution was made by I.F. Sbalzarini and coworkers (14), who proposed to infer point interaction properties from parametric models of spatial interaction (see Fig. 4D). They modeled the interaction between points $1 \leq i \leq n_1$ and $1 \leq j \leq n_2$ with a Gibbs process whose probability density $p(X, Y)$ is related to point positions $\mathbf{x}_i$ and $\mathbf{y}_j$ through the Boltzmann distribution $p(X,Y) \propto \exp(-\sum_{i=1}^{n_1}\sum_{j=1}^{n_2} \Phi(\mathbf{x}_i, \mathbf{y}_j))$, where $\Phi(\mathbf{x}_i, \mathbf{y}_j))$ is the interacting potential between points $\mathbf{x}_i$ and $\mathbf{y}_j$. Then, assuming that only nearest-neigbors can interact, they parametrized

$\Phi(\mathbf{x}_i, \mathbf{y}_j) = \epsilon f\left(\frac{d_{ij}-a}{b}\right)$ where ϵ is the interaction strength ($\epsilon = 0$ corresponds to noninteracting particles), b the interaction length scale and a a shift along the distance axis of the interaction potential. Finally, based on the observed distances $D = (d_i)_{i=1..n_1}$ of A_1 points to nearest neighbors, they estimated the interaction parameters $\hat{\epsilon}, \hat{b}$ and $\hat{a}$ thanks to maximum-likelihood estimation. Importantly, they also tested the statistical relevance of the estimated parameters. Indeed, $\hat{\epsilon} > 0$ does not imply necessarily that there are true interactions between points ($\epsilon > 0$). Thus, using Monte-Carlo re-sampling in the FOV, they assessed the statistical relevance of the computed parameters by estimating the maximum values that parameters can reach with given probability α under the null hypothesis of no interaction.

To the best of our knowledge, there is no such parametric fitting method for the Ripley's K function. Indeed, many models have been developed over years to analyze the clustering of a single population of points but not for the colocalization of two populations of points. In classical single population models, parent points are distributed in the FOV and then, offspring points are distributed around parents to form clusters. Cluster models then specify the (random) number of offsprings per parent, and the spatial distributions of parents and offsprings. For example, in the Matérn cluster process, parents are randomly distributed (homogeneous Poisson process) and have a Poisson number of offsprings, that are independently and uniformly distributed in a disc of radius r centered around the parent (50). Another example is given by the Thomas process, where the spatial distribution of offsprings around parents is Gaussian. However, only few models accounting for the interaction distance d_{ij} between two interacting point populations $\mathbf{x}_i$ and $\mathbf{y}_j$ have been developed.

In this review, we adapted the Thomas process for two populations and modeled the interaction distance between A_1 and A_2 points with a Gaussian distribution: $d_{ij} \sim \mathcal{N}(a, b)$. The Gaussian mean a results from the interaction distance and potential mis-alignment between channels, and the standard deviation b models the possible variations of the interaction distance and molecule localization errors (32). Assuming that a percentage p_2 of A_2 points colocalize with A_1 points, and that the other $(1-p_2)n_2$ A_2 points are randomly distributed in the FOV, we computed that $\mathbb{E}\{S(r)|p_2, a, b\} = B(r) + p_2 \frac{|\Omega|}{2n_1}\left(\mathrm{erf}\left(\frac{r-a}{\sqrt{2}b}\right) - \mathrm{erf}\left(\frac{-r-a}{\sqrt{2}b}\right)\right)$, where erf is the error function. We could then estimate p_2, b, and a by fitting the empirical $S(r)$ with the theoretical mean curve $\mathbb{E}\{S(r)|p_2, a, b\}$ (see Fig. 4D).

We finish by noting that previous methods are parametric, and thus are afflicted with the standard issues associated with model embedding, such as choosing an adapted and sufficiently general model, or checking the goodness of fit in a robust way. Development of nonparametric methods thus constitutes a promising research direction that would allow to extract colocalization parameters without these drawbacks.

Comparing Pixel- and Object-Based Methods on Synthetic and Biological Images

Synthetic Images

We compared how pixel-based and object-based methods performed on synthetic fluorescence images with different (known) percentage of molecule colocalization. We generated the synthetic images by using a Mixed Poisson-Gaussian model (see chapter 1 of Ref. 20 and Material and Methods). We modeled molecule colocalization with a Thomas process (see subsection "Quantitative interpretation"), the colocalization distance following a Gaussian distribution with mean $a = 0$ or $a = 1$ pixel and standard deviation $b = 0.3$. We then varied the percentage $p_2 = 0, 5, 10, 25, 50,$ and 75%, or $p_2 = 100\%$ of A_2 molecules ($n_2 = 100$) that colocalize with A_1 molecules ($n_1 = 100$). The FOV Ω is a 256 $\times$ 256 pixels square. We also generated images with no noise. Synthetic images with different levels of noise and spot colocalization were generated by using the plugin Colocalization Simulator implemented in Icy. To analyze molecule colocalization, we implemented and used the plugin Colocalization Studio that contains pixel-based methods that were introduced in section "Pixel-Based Methods," and Ripley-based analysis. For the object-based method, we first extracted molecule spots with wavelet-based denoising (see Material and Methods and Fig. 5).

First, concerning the statistical analysis of molecule colocalization, we computed the Pearson and the Manders correlation coefficients for each colocalization percentage and experiment ($M = 10$). We then tested the statistical significance of the Pearson and Manders with spots randomization ($N = 500$ simulations). We did not use here ICQ analysis (27) because simulated signal intensity was low, leading to an assymetric fluorescence intensity distribution (skewness > 0) and many false positives with ICQ analysis (see subsection "Statistical robustness"). For object-based methods, we computed the zero-mean and unit-variance, Ripley-based statistics $\tilde{S}(r) = (S(r) - \mu(r))/\sigma(r)$ (see subsection IV B). We showed that $\tilde{S}(r)$ is normally distributed $\tilde{S}(r) \sim \mathcal{N}(0, 1)$ (15), and its critical quantiles $q_{1-\alpha}(r)$ under the null hypothesis of A_2 random distribution are thus equal to the quantile $z_{1-\alpha}$ of $\mathcal{N}(0, 1)$. Thus, we computed the P values of molecule colocalization for each experiment with formula P value $= cdf(\max_{0 \le r \le r_{max}} \tilde{S}(r))$, where cdf is the cumulative density function of the standard normal law $\mathcal{N}(0, 1)$. We found that colocalization was robustly assessed with both pixel- and object-based methods, in every experimental condition (with or without noise and pixel shift between colocalized spots; see Fig. 5). Indeed, spot-randomization in pixel-based methods, and analytical formula of $\tilde{S}(r)$ quantiles did not reject the null hypothesis of molecule random distribution for $P_2 = 0\%$. In particular, Pearson and Manders P-values were very close to each other in every experimental condition: p value $\approx 0.5 \pm 0.1$(standarderror) with noise and P value $\approx 0.35 \pm 0.08$ without noise. Ripley-based analysis led to slightly higher and more homogeneous P values: P value $\approx 0.6 \pm 0.03$ with or without noise. In contrast, for $P_2 \ge 5\%$ we found

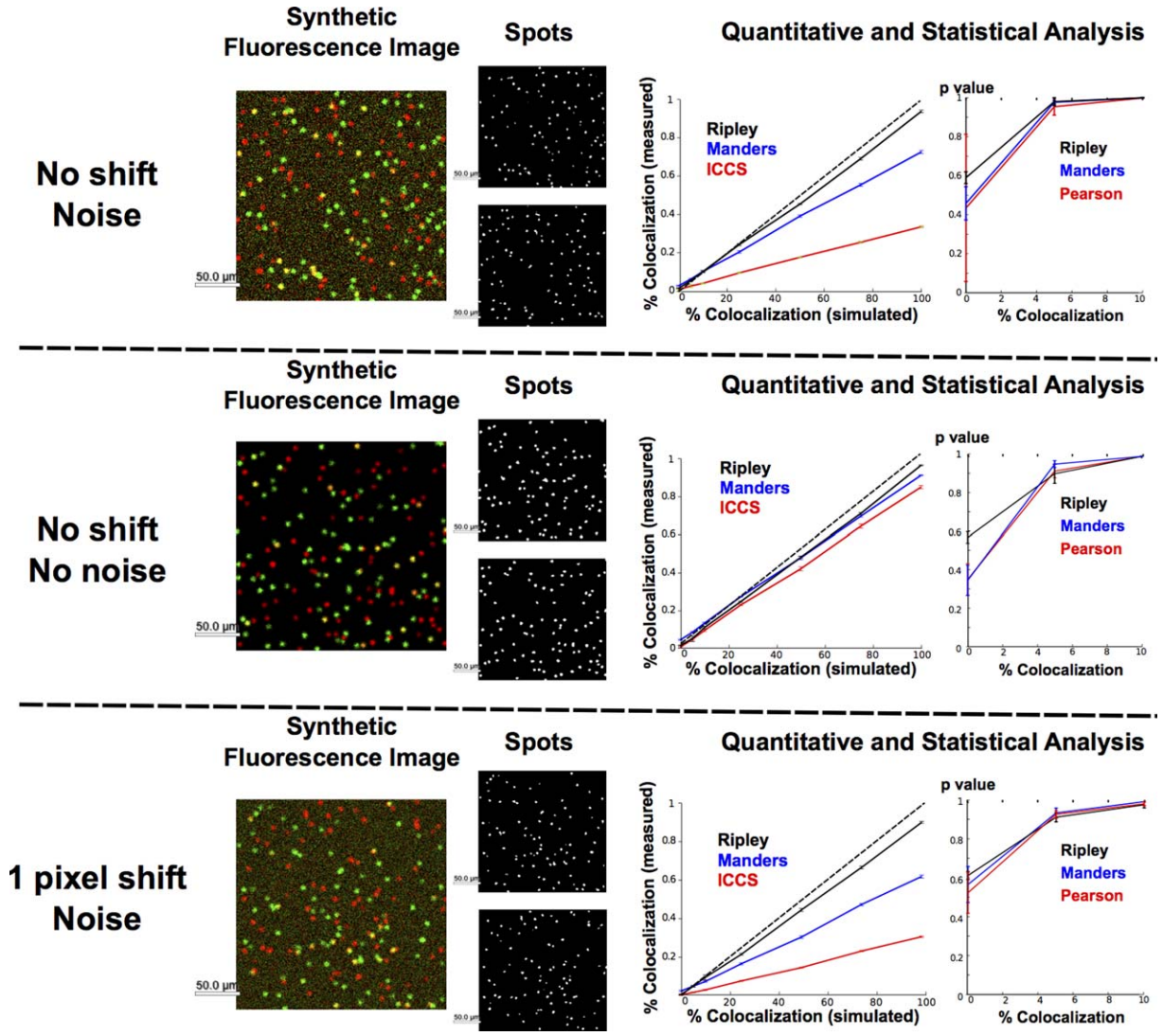

Figure 5. Method comparison with synthetic images dual-color synthetic images with $n_1 = n_2 = 100$ spots are generated with a Poisson-Gaussian model (see Material and Methods). Fluorescent spots are then automatically segmented with a wavelet-based algorithm (22). Percentage of colocalization [mean ± standard error ($N = 10$ simulations)] estimated with pixel-based methods {Manders coefficient (9) (solid blue line) and ICCS (35,36) (red blue line)} or object-based method [parametric fitting of the Ripley's K function (solid black line)] is compared with the simulated percentage of colocalization. The dashed black line represents the function $y = x$, corresponding to an ideal matching between simulated and estimated percentages of colocalization. Statistical significance [mean P values ± standard errors ($N = 500$ simulations)] of pixel-based methods {Manders (9) (solid blue line) and Pearson (10) (red blue line)} correlation coefficients are obtained with spot randomization. In Ripley based method (solid black line), the statistical analysis is based on the comparison of the maximum of the zero-mean and unit-variance, Ripley-based statistics $\tilde{S}(r)$ with quantiles of the standard normal law (15). [Color figure can be viewed in the online issue, which is available at wileyonlinelibrary.com.]

that Pearson, Manders and Ripley P-values are very close to each other, and above 90% indicating spot colocalization unambiguously.

Concerning the quantification analysis, we used Manders overlap coefficients and ICCS analysis as pixel-based methods (see subsection "Quantitative interpretation"), and we also fitted object-based function $\tilde{S}(r)$ with its parametric mean $\mathbb{E}\{\tilde{S}(r)|p_2, a, b\}$ obtained from a Thomas process (see subsection "Colocalization Quantification"). We observed in Figure 5 that all methods under-estimated the simulated percentage of colocalization (curves below the function $y = x$), but that Ripley-based analysis was far more accurate (relative error < 10% in every experimental condition and simulated colocalization percentage) than Manders and ICCS analysis. In particular, we observed that Manders and ICCS analysis were significantly affected by image noise and shifting between colocalized spots, relative errors between simulated and estimated percentages of colocalization reaching $\approx 40-50\%$ for Manders overlap coefficients, and $\approx 70\%$ for ICCS analysis. In contrast, Manders and ICCS analysis were much more accurate in images with no noise (relative errors <10% and <20% for Manders and ICCS analysis respectively). ICCS sensitivity to noise has also been highlighted by Wu et al. (36). Overall, these simulations demonstrate the importance of

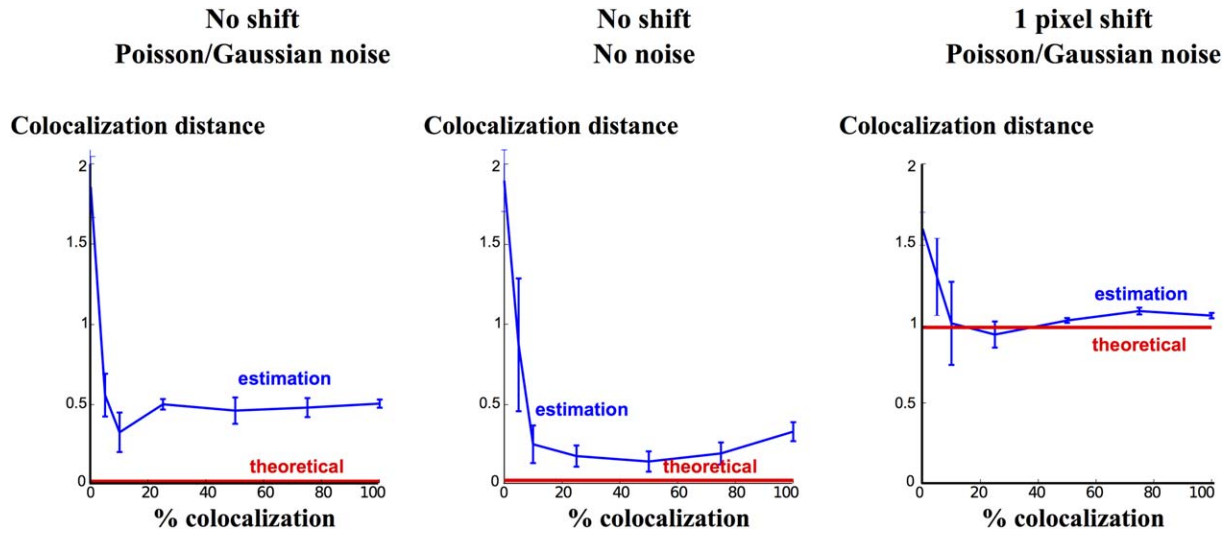

Figure 6. Estimation of colocalization distance with Ripley-based analysis. Dual-color synthetic images with $n_1 = n_2 = 100$ spots are generated with a Poisson-Gaussian model (see Material and Methods). Fluorescent spots are then automatically segmented with a wavelet-based algorithm ((22)). Colocalization distance is estimated [solid blue line, mean ± standard error ($N = 10$ simulations)] by fitting the Ripley's K function to a parametric Thomas model (see subsection IV C). The theoretical mean distance (solid red line) corresponds to the pixel shift between the colocalized spots. [Color figure can be viewed in the online issue, which is available at wileyonlinelibrary.com.]

image denoising and deconvolution before using pixel-based methods. Finally, we also found (data not shown) that, for no spot colocalization $P_2 = 0\%$, Manders overlap coefficients increase almost linearly with spot density: $M_1 = M_2 = 0.02 \pm 0$ for $n_1 = n_2 = 100$ and $M_1 = M_2 = 0.062 \pm 0.005$ for $n_1 = n_2 = 300$. This highlights that Manders coefficients have to be used consciensously in images with high spot density due to fortuitous spot overlap that can lead to colocalization overestimation.

We also used $\tilde{S}(r)$ fitting to estimate the mean distance a between colocalized molecules (see Fig. 6). For images with no shift between colocalized spots, we found that a was slightly overestimated to $a \approx 0.5 \pm 0.1$ with noise and $a \approx 0.25 \pm 0.1$ without noise. These estimates were obtained when the percentage of colocalization was sufficiently high (>10%) to ensure a robust estimation. Estimation overestimation is likely due to molecule localization errors, which explains the better accuracy of a estimation in images with no noise where localization accuracy is increased (32). For images with 1 pixel-shift, a estimation was more precise $a \approx 1.05 \pm 0.02$, which may be due to the fact that localization errors are then small compared with molecule shift (32).

Biological Images

We analyzed the colocalization of two endocytic cargos, Tf and IL-2R, with intracellular molecules that are implicated in different endocytic pathways. Endocytosis is a key receptor-mediated mechanism that regulates the entry of signaling molecules and nutrients from the extra-cellular medium into the cell, and the uptake of Tf and IL-2 regulate respectively the iron uptake (51) and the proliferation of T cells during the cell mediated immunity (52,53). There are several endocytic pathways, and the most well known is mediated by the clathrin protein that forms coats around specific receptors, leading to membrane invagination and molecule entry. Another important entry pathway is mediated by the caveolin, and it is well known that Tf uses the clathrin pathway (54), and not the caveolin pathway. In addition, it has been shown that the internalization of IL-2R is clathrin-independent (55,56). Here, we assess these different interactions by quantifying the co-localization between the two endocytic cargos (Tf and IL-2R) and the intracellular clathrin molecules, and between the Tf and the intracellular caveolin molecule in Total Internal Reflexion Fluorescence (TIRF) microscopy (see Fig. 7), which restricts the observation plasma membrane proximity (∼150 nm depth).

Using pixel-based methods, we found a statistical colocalization between Tf and clathrin (Pearson coefficient $R = 0.62 \pm 0.09$ ($n = 3$), P-value (pixel randomization) $= 1 \pm 0$ and ICQ $= 0.221 \pm 0.05$, P-value $= 1 \pm 0$). This colocalization was confirmed by Van Steensel's shifting technique [implemented in the *Jacop* plugin (8) in ImageJ (57)], which demonstrated that R reached its maximum for a shift $\delta x = 0.66 \pm 0.33$ pixels. In addition, we also found with pixel randomization, but not with ICQ, which gave a false positive, that Tf and caveolin were not colocalized (Pearson coefficient $R = 0.05 \pm 0.02$ ($n = 3$), P-value (randomization) $= 0.76 \pm 0.13$. Finally false positive colocalization was found for IL-2R and clathrin with both pixel randomization and ICQ sign test. This may be due to local increase of (diffuse) signal intensities in some parts of the cells, such as in the bottom left of the FOV represented in Figure 7.

The statistical analysis was more robust with object-based method. Indeed, zero-mean and unit variance Ripley's K function $\tilde{S}(r)$ reached a mean maximum value of 7.33 ± 1.85 (P-value $= 1 \pm 0.0$) for Tf and clathrin colocalization. In contrast, $\tilde{S}(r)$ maximum was only of 0.15 ± 0.07 (P-value $= 0.56 \pm 0.03$) and 0.34 ± 0.17 (P value $= 0.63 \pm 0.06$) for Tf/caveolin and IL-2R/clathrin, respectively.

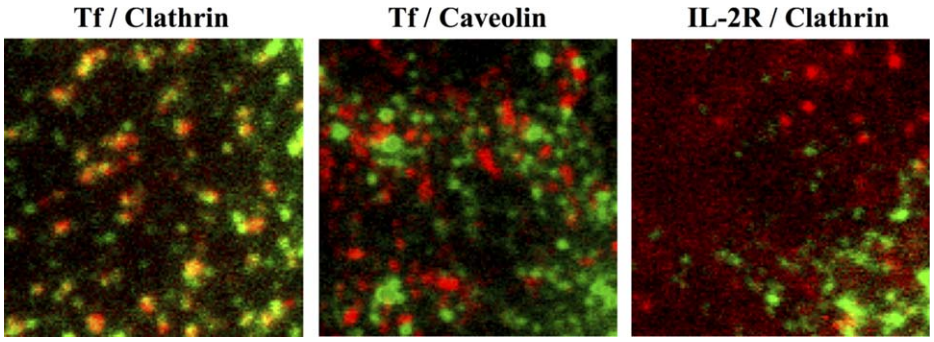

Figure 7. TIRF imaging of endocytic cargos and intracellular molecules. Green Fluorescent Proteins (GFP)-tagged clathrin-light chain (CLC) and caveolin 1 (18,19) were transfected into Hep2β cells (19). Tf and IL-2Rβ antibody were then labeled with fluorescent red dye Cy3 and imaged in TIRF microscopy. [Color figure can be viewed in the online issue, which is available at wileyonlinelibrary.com.]

Concerning colocalization quantification, we found that, due to high level of diffuse signal and molecule densities, Manders' coefficients were relatively elevated for noncolocalized molecules: $M_1 = 0.22 \pm 0.01, M_2 = 0.26 \pm 0.04$ for Tf/caveolin, and $M_1 = 0.18 \pm 0.11, M_2 = 0.12 \pm 0.05$ for IL-2R/clathrin. In contrast, ICCS analysis confirmed that Tf and caveolin do not colocalize ($P_1 = 3 \pm 1\%, P_2 = 9 \pm 3\%$), but colocalization percentages were relatively high for IL-2R/clathrin ($P_1 = 5 \pm 3.7\%, P_2 = 17 \pm 14\%$). Parametric fit of Ripley's K function $\tilde{S}(r)$ confirmed that neither Tf and caveolin ($P_1 = P_2 = 3.8 \pm 2.1\%$), nor IL-2R and clathrin ($P_1 = 3.3 \pm 1.8\%, P_2 = 5 \pm 2.5\%$) colocalize. Regarding Tf and clathrin, Manders correlation coefficients ($M_1 = 0.74 \pm 0.04$, $M_2 = 0.49 \pm 0.14$), ICCS analysis ($P_1 = 86 \pm 19\%, P_2 = 46 \pm 6.7\%$) and object-based method ($P_1 = 59 \pm 6.4\%$, $P_2 = 42 \pm 10\%$) all corroborated a high level of colocalization. Moreover, by fitting $\tilde{S}(r)$ with Thomas process mean curve, we found that colocalization distance between Tf and clathrin was relatively small $a = 0.78 \pm 0.26$ pixels, corresponding to a mean distance of 70 ± 23 nm.

Conclusion

In this review, we have presented the main colocalization methods, which are divided into pixel-based and object-based. We have compared these different methods on synthetic and biological images, and found that object-based methods perform much better than pixel-based methods. Indeed, statistical analysis in object-based methods is as robust as in pixel-based methods, but does not require spot randomization because the analytical quantiles of the Ripley's K function are known. We also found that object-based methods quantified more accurately the percentage of colocalized molecules than pixel-based methods, and were not sensitive to image noise and pixel-shift between colocalized molecules. Finally, we showed that the mean distance between colocalized molecules can be robustly inferred from the parametric fitting of the Ripley's K function in object-based methods.

Object-based methods apply when molecule signals are spotty, making their individual detection and representation possible as points in the delimited FOV. However, due to molecule density, intensity signal can become diffuse and molecule individualization difficult and in this case pixel-based methods are better-suited to measure signal correlations. Moreover, in many biological applications, each intensity peak corresponds to an unknown number of fluorescence molecules. In this situation, pixel-based methods may perform better because the linear relationship between pixel intensity and number of molecules is preserved. In contrast, this relationship is not valid in object-based methods due to preliminary spot segmentation and representation as points. However, we highlight that new single molecule techniques in fluorescence microscopy allow to infer statistically the number of molecules per fluorescent spot from peak intensity (58,59). Then, weighting each point with the computed number of molecules per peak would be a promising extension of Marked Point Processes (41) in object-based methods to tackle this issue.

Finally, other important technical issues remain unsolved in object-based methods. First, there is no analytical test of molecule colocalization that accounts globally for the multidistance information $S(r_i), r_1 < \ldots r_i < \ldots < r_N$. Indeed, second-order statistics (Nearest-Neighbor or Ripley's K functions) $S(r_i)$ and $S(r_j)$, for $1 \leq i \neq j \leq N$, are correlated random variables, and for now, their covariance can only be accessed with Monte-Carlo simulations (14). A first challenge would be to compute these co-variances analytically, and this would open the way to robust and rapid multidistance test of colocalization, providing the precise probability that observed molecules are randomly distributed. Second, quantitative interpretation of $S(r)$ depends on model fitting, and is thus plagued with standard issues associated with model embedding, like checking the robustness of the fit and choosing a sufficiently general colocalization model. Developing nonparametric methods for the quantitative interpretation of $S(r)$ variations thus constitutes as well an important challenge.

Literature Cited

1. Doherty GJ, McMahon HT. Mechanisms of endocytosis. Annu Rev Biochem 2009; 78:857–902.
2. Fredlund J, Enninga J. Cytoplasmic access by intracellular bacterial pathogens. Trends Microbiol 2014;22:128–137.
3. Mercer J, Schelhaas M, Helenius A. Virus entry by endocytosis. Annu Rev Biochem 2010;79:803–833.
4. Valeur B, Berberan-Santos M. Excitation Energy Transfer. Molecular Fluorescence: Principles and Applications. Weinheim, Germany: Wiley-VCH; 2012.

5. Schwille P, Meyer-Almes FJ, Rigler R. Dual-color fluorescence cross-correlation spectroscopy for multicomponent diffusional analysis in solution. Biophys J 1997;72: 1878–1886.
6. Fletcher PA, Scriven DRL, Schulson MN, Moore EDW. Multi-image colocalization and its statistical significance. Biophys J 2010;99:1996–2005.
7. Levenson R, Hoyt C. Spectral imaging and microscopy. Am Lab 2000;32:26–34.
8. Bolte S, Cordelieres FP. A guided tour into subcellular colocalization analysis in light microscopy. J Microsc 2006;224:213–232.
9. Manders E, Verbeek F, Aten J. Measurement of co-localization of objects in dual-colour confocal images. J Microsc 1993;169:375–382.
10. Costes SV, Daelemans D, Cho EH, Dobbin Z, Pavlakis G, Lockett S. Automatic and quantitative measurement of protein-protein colocalization in live cells. Biophys J 2004;86:3993–4003.
11. Lachmanovich E, Shvartsman DE, Malka Y, Botvin C, Henis YI, Weiss AM. Co-localization analysis of complex formation among membrane proteins by computerized fluorescence microscopy: Application to immunofluorescence co-patching studies. J Microsc 2003;212:122–131.
12. Prior IA, Muncke C, Parton RG, Hancock JF. Direct visualization of ras proteins in spatially distinct cell surface microdomains. J Cell Biol 2003;160:165–170.
13. Zhang B, Chenouard N, Olivo-Marin JC, Meas-Yedid V. Statistical colocalization in biological imaging with false discovery control. In: IEEE International Symposium on Biomedical Imaging ISBI, Paris, 2008. pp 1327−1330.
14. Helmuth JA, Paul G, Sbalzarini IF. Beyond co-localization: Inferring spatial interactions between sub-cellular structures from microscopy images. BMC Bioinformatics 2010;11:372
15. Lagache T, Meas-Yedid V, Olivo-Marin JC. A statistical analysis of spatial colocalization using ripley's k function. In: IEEE International Symposium on Biomedical Imaging ISBI, San Francisco, 2013. pp 896–901.
16. Rossy J, Cohen E, Gaus K, Owen DM. Method for co-cluster analysis in multichannel single-molecule localisation data. Histochem Cell Biol 2014;141:605–612.
17. Grassart A, Dujeancourt A, Lazarow PB, Dautry-Varsat A, Sauvonnet N. Clathrin-independent endocytosis used by the il-2 receptor is regulated by rac1, pak1 and pak2. EMBO Rep 2008;9:356–362.
18. Ewers H, Smith AE, Sbalzarini IF, Lilie H, Koumoutsakos P, Helenius A. Single-particle tracking of murine polyoma virus-like particles on live cells and artificial membranes. Proc Natl Acad Sci USA 2005;102:15110–15115.
19. Basquin C, Malardé V, Mellor P, Anderson DH, Meas-Yedid V, Olivo-Marin JC, Dautry-Varsat A, Sauvonnet N. The signalling factor pi3k is a specific regulator of the clathrin-independent dynamin-dependent endocytosis of il-2 receptors. J Cell Sci 2013;126(Pt 5):1099–1108.
20. Chenouard N. Advances in probabilistic particle tracking. Ph.D. thesis, Institut Pasteur & TelecomParisTech, 2010.
21. Zhang B, Zerubia J, Olivo-Marin JC. Gaussian approximations of fluorescence microscope point-spread function models. Appl Opt 2007;46:1819–1829.
22. Olivo-Marin JC. Extraction of spots in biological images using multiscale products. Pattern Recognit 2002;35:1989–1996.
23. de Chaumont F, Dallongeville S, Chenouard N, Hervé N, Pop S, Provoost T, Meas-Yedid V, Pankajakshan P, Lecomte T, Le Montagner Y, et al. Icy: An open bioimage informatics platform for extended reproducible research. Nat Methods 2012;9:690–696.
24. van Steensel B, van Binnendijk EP, Hornsby CD, van der Voort HT, Krozowski ZS, de Kloet ER, van Driel R. Partial colocalization of glucocorticoid and mineralocorticoid receptors in discrete compartments in nuclei of rat hippocampus neurons. J Cell Sci 1996;109:787–792.
25. Lifshitz LM. Determining data independence on a digitized membrane in three dimensions. IEEE Trans Med Imaging 1998;17:299–303.
26. Demandolx D, Davoust J. Multicolour analysis and local image correlation in confocal microscopy. J Microsc 1997;185:21–36.
27. Li Q, Lau A, Morris TJ, Guo L, Fordyce CB, Stanley EF. A syntaxin 1, galpha(o), and n-type calcium channel complex at a presynaptic nerve terminal: Analysis by quantitative immunocolocalization. J Neurosci 2004;24:4070–4081.
28. McDonald JH, Dunn KW. Statistical tests for measures of colocalization in biological microscopy. J Microsc 2013;252:295–302.
29. Dunn KW, Kamocka MM, McDonald JH. A practical guide to evaluating colocalization in biological microscopy. Am J Physiol Cell Physiol 2011;300:C723–C742.
30. Ramírez O, García A, Rojas R, Couve A, Härtel S. Confined displacement algorithm determines true and random colocalization in fluorescence microscopy. J Microsc 2010;239:173–183.
31. Wang Y, Ledgerwood C, Grills C, Fitzgerald DC, Hamilton PW. A robust co-localisation measurement utilising z-stack image intensity similarities for biological studies. PLoS One 2012;7:e30632
32. Thompson RE, Larson DR, Webb WW. Precise nanometer localization analysis for individual fluorescent probes. Biophys J 2002;82:2775–2783.
33. Gustafsson MGL. Nonlinear structured-illumination microscopy: Wide-field fluorescence imaging with theoretically unlimited resolution. Proc Natl Acad Sci USA 2005; 102:13081–13086.
34. Hell SW, Wichmann J. Breaking the diffraction resolution limit by stimulated emission: Stimulated-emission-depletion fluorescence microscopy. Opt Lett 1994;19:780–782.
35. Comeau JWD, Costantino S, Wiseman PW. A guide to accurate fluorescence microscopy colocalization measurements. Biophys J 2006;91:4611–4622.
36. Wu Y, Eghbali M, Ou J, Lu R, Toro L, Stefani E. Quantitative determination of spatial protein-protein correlations in fluorescence confocal microscopy. Biophys J 2010;98: 493–504.
37. Betzig E, Patterson GH, Sougrat R, Lindwasser OW, Olenych S, Bonifacino JS, Davidson MW, Lippincott-Schwartz J, Hess HF. Imaging intracellular fluorescent proteins at nanometer resolution. Science 2006;313:1642–1645.
38. Rust MJ, Bates M, Zhuang X. Sub-diffraction-limit imaging by stochastic optical reconstruction microscopy (storm). Nat Methods 2006;3:793–795.
39. Thomann D, Rines DR, Sorger PK, Danuser G. Automatic fluorescent tag detection in 3d with super-resolution: application to the analysis of chromosome movement. J Microsc 2002;208(Pt 1):49–64.
40. Smal I, Loog M, Niessen W, Meijering E. Quantitative comparison of spot detection methods in fluorescence microscopy. IEEE Trans Med Imaging 2010;29:282–301.
41. Illian J, Penttinen A, Stoyan H, Stoyan D. Statistical Analysis and Modelling of Spatial Point Patterns. Chichester, UK: Wiley, 2008.
42. Clark P, Evans FC. Distance to nearest neighbour as a measure of spatial relationships in populations. Ecology 1954;35:445–453.
43. Ripley B. The second-order analysis of stationary point processes. J Appl Probability 1976;13:255–266.
44. Chandler D. Introduction to Modern Statistical Mechanics. New York: Oxford University Press; 1987.
45. Wieg T, Moloney KA. Rings, circles, and null-models for point pattern analysis in ecology. Oikos 2004;104:209–229.
46. Torquato Lu, Rubinstein. Nearest-neighbor distribution functions in many-body systems. Phys Rev A 1990;41:2059–2075.
47. Lang G, Marcon E. Testing randomness of spatial point patterns with the ripley statistic. ESAIM: Probability Stat 2013;17:767–788.
48. Ripley B. Statistical inference for spatial processes. New York: Cambridge University Press; 1988.
49. Donnelly K. Simulations to determine the variance and edge-effect of total nearest neighbour distance. In Simulation methods in archaeology. New York: Cambridge University Press; 1978.
50. Matèrn B. Poisson processes in the plane and related models for clumping and heterogeneity. Ph.D. thesis, NATO Advanced Study Institute on Statistical Ecology. Pennsylvania State University, 1972.
51. Dautry-Varsat A. Receptor-mediated endocytosis: the intracellular journey of transferrin and its receptor. Biochimie 1986;68:375–381.
52. Gesbert F, Sauvonnet N, Dautry-Varsat A. Clathrin-lndependent endocytosis and signalling of interleukin 2 receptors il-2r endocytosis and signalling. Curr Top Microbiol Immunol 2004;286:119–148.
53. Liao W, Lin JX, Leonard WJ. Il-2 family cytokines: new insights into the complex roles of il-2 as a broad regulator of t helper cell differentiation. Curr Opin Immunol 2011;23:598–604.
54. Hanover JA, Willingham MC, Pastan I. Kinetics of transit of transferrin and epidermal growth factor through clathrin-coated membranes. Cell 1984;39(2 Pt 1):283–293.
55. Lamaze C, Dujeancourt A, Baba T, Lo CG, Benmerah A, Dautry-Varsat A. Interleukin 2 receptors and detergent-resistant membrane domains define a clathrin-independent endocytic pathway. Mol Cell 2001;7:661–671.
56. Sauvonnet N, Dujeancourt A, Dautry-Varsat A. Cortactin and dynamin are required for the clathrin-independent endocytosis of gammac cytokine receptor. J Cell Biol 2005;168:155–163.
57. Schneider CA, Rasb WS, Eliceiri KW. Nih image to imagej: 25 years of image analysis. Nat Methods 2012;9:671–675.
58. Kasai RS, Suzuki KGN, Prossnitz ER, Koyama-Honda I, Nakada C, Fujiwara TK, Kusumi A. Full characterization of gpcr monomer-dimer dynamic equilibrium by single molecule imaging. J Cell Biol 2011;192:463–480.
59. Grassart A, Cheng AT, Hong SH, Zhang F, Zenzer N, Feng Y, Briner DM, Davis GD, Malkov D, Drubin DG. Actin and dynamin2 dynamics and interplay during clathrin-mediated endocytosis. J Cell Biol 2014;205:721–735.